Sciencexpress Reports

Observation of a periodic array of flux-closure quadrants in strained ferroelectric $PbTiO_3$ films

Y. L. Tang,[1]* Y. L. Zhu,[1]* X. L. Ma,[1]† A. Y. Borisevich,[2] A. N. Morozovska,[3] E. A. Eliseev,[4] W. Y. Wang,[1] Y. J. Wang,[1] Y. B. Xu,[1] Z. D. Zhang,[1] S. J. Pennycook[5,6]

[1]Shenyang National Laboratory for Materials Science (SYNL), Institute of Metal Research, Chinese Academy of Sciences, Wenhua Road 72, 110016 Shenyang, China. [2]Oak Ridge National Laboratory, Materials Science and Technology Division, Oak Ridge, TN 37831-6071, USA. [3]Institute of Physics, National Academy of Sciences of Ukraine, 46 pr. Nauky, 03028 Kyiv, Ukraine. [4]Institute for Problems of Materials Sciences, National Academy of Sciences of Ukraine, 3 Krjijanovskogo, 03142 Kyiv, Ukraine. [5]Department of Materials Science and Engineering, University of Tennessee, Knoxville, TN 37996-2200, USA. [6]Department of Materials Science and Engineering, National University of Singapore, Singapore 117576, Singapore.

*These authors contributed equally to this work.

†Corresponding author. E-mail: xlma@imr.ac.cn

Nanoscale ferroelectrics are expected to exhibit various exotic domain configurations, such as the full flux-closure pattern that is well known in ferromagnetic materials. Here we observe not only the atomic morphology of the flux-closure quadrant but also a periodic array of flux closures in ferroelectric $PbTiO_3$ films, mediated by tensile strain on a $GdScO_3$ substrate. Using aberration-corrected scanning transmission electron microscopy, we directly visualize an alternating array of clockwise and counterclockwise flux closures, whose periodicity depends on the $PbTiO_3$ film thickness. In the vicinity of the core, the strain is sufficient to rupture the lattice, with strain gradients up to 10^9 per meter. Engineering strain at the nanoscale may facilitate the development of nanoscale ferroelectric devices.

Atomic-scale information is of critical importance for understanding intrinsic characteristics of advanced functional materials such as ferroelectrics, magnets, superconductors, and catalysts. For example, it is often the small deviations from symmetry in atom positions and the resultant strains that allow ferroelectric oxides, used in computer memory chips, to store charge and information or to resonate with magnets as composite multiferroics. Ferroelectric crystals feature asymmetric or polar structures that are switchable under an external field, holding promise for random access memories, thin-film capacitors, and actuators (*1*). For integration into silicon chips, practical ferroelectric memories take the form of nanoscale films (*1*). Nanoscale ferroelectrics have been predicted to undergo unusual phase transitions and exhibit distinctive domain patterns, such as closure quadrants with closed head-tail dipole moments, known as flux closures (*2*–*7*). These flux-closure domains should be switchable and may give rise to an unusually high density of bits (*2*), and they can undergo vortex-polarization phase transformation (*6*). These domains are also predicted to be potentially useful as mechanical sensors and transducers (*7*). Similar domains are well known in ferromagnetic materials (*8*–*10*), and their topological properties and dynamics are under investigation (*9*, *10*). However, in ferroelectric materials, particularly in tetragonal ferroelectrics, the coupling of polarization to spontaneous strain would be so pronounced that formation of a closure quadrant with its resultant severe disclination strains could be impossible (*11*, *12*). Although closure quadrants were reported recently in tetragonal ferroelectric $BaTiO_3$ (*13*–*16*), $PbZr_{0.42}Ti_{0.58}O_3$ (*17*), and PZN-12PT (*18*), they are mostly composed of shape-conserving 90° stripe domains or twins within each quadrant to accommodate the disclination strains. In such cases, the closure quadrants may not always involve continuous dipole rotations, as have been observed directly in half of a closure quadrant in $PbZr_{0.2}Ti_{0.8}O_3$ (*19*) and $BiFeO_3$ (*20*) by aberration-correction transmission electron microscopy (TEM) or scanning TEM (STEM). The atomic-scale characterization based on STEM imaging has been validated to be capable of directly displaying ionic displacement maps (*19*–*24*), whereas approaches based on piezoresponse force microscopy are not able to do so because of lower spatial resolution (*11*, *14*–*18*, *25*, *26*).

In this study, we have grown $PbTiO_3$/$SrTiO_3$ (PTO/STO) multilayer films on a $GdScO_3$ substrate with a lattice parameter larger than the *a* value of PTO (*27*). Using aberration-corrected high-angle annular dark-field (HAADF) *Z*-contrast STEM imaging, we visualize, at the atomic scale, the existence of periodic twin-free flux-closure quadrants.

$PbTiO_3$ has a tetragonal structure (Fig. 1A). Both the oxygen octahedra and the Ti^{4+} have displacements from the center of the Pb^{2+} tetragonal cell that give rise to the spontaneous polarization (Fig. 1, B and C). The shifts of Ti^{4+} (denoted as δ_{Ti} in Fig. 1B) can be used to determine the polarizations of PTO unit cells. In HAADF images, the Pb^{2+} columns appear as the brightest dots because the intensity of atom columns is approximately proportional to Z^2, where *Z* is the atomic number (*20*, *21*, *23*, *24*). The Ti^{4+} columns show weaker contrast. The displacement vectors of Ti^{4+} (δ_{Ti})

relative to the center of mass of the four nearest Pb^{2+} neighbors (Fig. 1C) can be determined by fitting them as two-dimensional (2D) Gaussian peaks, based on the HAADF-STEM images (*19*–*24*, *27*, *28*). The δ_{Ti} vector in each unit cell is opposite to the polarization direction of PTO (Fig. 1 and figs. S1 and S2).

A low-magnification high-resolution HAADF-STEM image of a PTO/STO film shows that the contrast in each PTO layer is basically uniform, indicating the homogeneity of chemical compositions (Fig. 1D). Slight variation of the contrast implies the existence of domain walls. The domain structure was characterized by geometric phase analysis (GPA) (*21*, *27*, *29*). The out-of-plane strain ε_{yy} shown in Fig. 1E displays a clear spatial arrangement of the domain patterns. The domains in the upper PTO layer (in red, *c* domains, with *c* axis along the out-of-plane direction) form a 2D periodic sinusoidal array, whereas the domains with triangular configurations give rise to another periodic array (in green, *a* domains, with *c* axis along the in-plane direction).

Four typical areas (labeled as 1, 2, 3, and 4 in Fig. 1D) are magnified in Fig. 2A, which shows the atomically resolved HAADF-STEM images corresponding to these four areas. The atomic structures in each image depict the positions of Ti^{4+} and Pb^{2+} columns by red and yellow circles, respectively. For example, on the left side of area 2, the δ_{Ti} is upward, whereas on the right side of the image, the δ_{Ti} is downward. The yellow arrows denote the reversed δ_{Ti} directions, which are also the directions of spontaneous polarization (*22*, *24*). The opposite local polarization directions indicate the presence of two domains in a 180° orientation relation; the corresponding domain walls are marked by red dashed lines. At the bottom interface of PTO/STO, in-plane δ_{Ti} vectors are discernable; thus two 90° domain walls are outlined (blue dashed lines). Such in-plane displacement may play an important role in stabilizing this ferroelectric domain configuration (*4*, *19*). The 90° domain walls for areas 1 and 4 are denoted by green dashed lines. Figure 2B displays a superposition of the $-\delta_{Ti}$ vectors mapping with the atomic images in Fig. 2A. The $-\delta_{Ti}$ vectors are marked with an arrow located at the Ti^{4+} columns. The combined δ_{Ti} configurations in areas 1 and 2 form a flux-closure pattern (closure quadrant); the same is true for combined areas 3 and 4. Such a closure configuration is almost the same as that predicted in ferromagnetic materials in (*12*) and in ferroelectrics in (*30*). The combination of 1 and 2 forms a counterclockwise flux closure, whereas the combination of 3 and 4 leads to a clockwise flux closure. The same closure patterns can be identified in other areas. Because the order parameter of each flux closure—the toroid moment **G**, defined by the sum of cross-multiplication of radial vector $\mathbf{R_i}$ and local dipole $\mathbf{p_i}$—can be uniquely assigned (*2*), an antiparallel configuration of the **G** can be determined for a periodic closure pattern. The dynamic interactions of the periodic closures are of technological importance, as explored recently in $BaTiO_3$ platelets, although the closures are still composed of shape-conserving 90° stripe domains within each quadrant to accommodate the disclination strains (*16*).

The long-range strains in these ferroelectric closure quadrants show interesting disclination characteristics. Based on the HAADF-STEM images, the in-plane and out-of-plane strains and lattice rotations [rigid-body rotation of crystal lattice (*21*, *29*)] are determined by GPA (Fig. 3). The *c* lattice strains (that is, the in-plane strain ε_{xx} in the triangle domains in Fig. 3, A to C, and the out-of-plane strain ε_{yy} in the sinusoidal array in Fig. 3, D to F) have a strong local maximum around the vertices of the triangle domains, leading to a giant *c* lattice strain gradient. Away from the vertex, the strain gradient estimated in the triangle domain is ~4×10^6 m^{-1} (Fig. 3C). The lattice rotations are also spatially inhomogeneous (Fig. 3, G to I); in each single domain, the lattice rotation changes continuously (Fig. 3, H and I). Sudden jumps of lattice rotations (red arrows in Fig. 3, H and I) can be used to locate the 180° domain walls in HAADF-STEM images. 3D illustrations of the *c* lattice strain mappings (fig. S3) indicate a giant strain gradient that appears like a "volcano" at the vertices of the flux closure.

Strains close to the vertex can be interpreted from the point of view of ferroelectric theory. Strains and strain gradients corresponding to the vertex derived from the HAADF images and calculated using the Landau-Ginsburg-Devonshire (LGD) framework are given in figs. S4 to S10. A strain gradient reaching ~10^9 m^{-1} near the vertices can be identified (fig. S5). The analysis of the results suggests that most of the considerable deformation that the material undergoes in the vicinity of the vertices (for instance, the peaks in Fig. 3, B and C) and around domain walls can be attributed to the ferroelectric-electrostrictive contribution, which is not surprising given the large *c*/*a* ratio of the $PbTiO_3$. However, the shear strain at the 180° domain wall appears to arise from a flexoelectric contribution

$$u_5 \approx \frac{-F_{44}P_S}{R_c \cosh^2\left(x_1/R_c\right)}$$

where u_5 is the shear strain component, F_{44} is a component of the flexoelectric tensor, P_S is the spontaneous polarization, R_c is the correlation radius (width of a domain wall), and x_1 is the coordinate normal to the 180° domain wall. In fact, the flexoelectric coefficient F_{44} can be directly estimated from the experimental data. The offset, which indicates the relative shift between two neighboring 180° domains, can be expressed as

$$\delta u_2 = 2F_{44}P_S$$

which is similar to the expression given in (*31*). Experimentally, we observe offsets as large as ~1.5 to 2 Å (fig. S11); together with the spontaneous polarization of 0.75 C m^{-2}, this gives us an estimate of $F_{44} \approx 10^{-10}$ C^{-1} m^3, which is within an order of magnitude of values previously reported (*31*, *32*).

Moreover, the lattice strain reaches extremely high val-

ues left and right of the core of the vertex (Fig. 2). At the core itself, the Pb columns appear to have bifurcated into two partial columns, possibly forming a small sliver of PbO. We expect large disclination stress in this region, the magnitude of which is roughly Eu, where E is Young's modulus and u is strain. The strain is much larger in the polar direction than in the nonpolar direction, consistent with the anisotropic elastic constants reported in (*33*). Using an average value of elastic constant c_{33} ~ 80 GPa in (*33*, *34*) as an estimate of E, with the observed dilatation reaching 25% in the core region, the stresses would appear to reach the order of 20 GPa. The theoretical shear strength σ_{theor} of a material can be estimated from

$$\sigma_{\text{theor}} = \sqrt{\frac{E\gamma}{a}}$$

where γ is the surface energy and a the lattice parameter. Using γ ~ 1 J m^{-2} (*35*) gives σ_{theor} ~ 14 GPa, suggesting that the lattice has ruptured because the disclination stresses exceeded the material's maximum shear strength. This lattice rupture is a general phenomenon at the vertex in this study (see fig. S12 for other examples).

For the whole multilayer structure, the periodic arrangement of the closure-quadrant arrays is characterized by two fundamental aspects. Structurally, the disclination pairs are arranged in a reversed manner, known as strain-compensating hetero-disclination pairs (*36*), whereas the clockwise and counterclockwise flux closures are stacked in an alternating fashion. This arrangement helps to relax the long-range strains in the disclinations (*36*), consequently stabilizing the closure quadrants. Nevertheless, a large strain gradient remains (Fig. 3). The disclination strain at the vertex here is up to 25%, which is more than one order of magnitude larger than that in rhombohedral $BiFeO_3$ ferroelectric, where the maximal disclination strain at the core is 1.5% (*26*). At the atomic level, our results show convincing evidence of the compatibility of disclinations and closure quadrants in a ferroelectric, even with strong tetragonality.

The periodic array of closure quadrants is occasionally absent in our PTO/STO multilayers. Figure 4A is a low-magnification TEM image of another PTO/STO film displaying an overview of the periodic array of the closure quadrants in both of the 20-nm PTO layers. Figure 4B shows a schematic illustration of the periodic closure quadrants.

By comparing PTO films with various thicknesses, we have derived the stabilization condition for such periodic closure quadrants (*27*). The thickness of each single PTO layer is the most important factor scaling the periodicity of the closure quadrants in tensile strained PTO/STO multilayers. We find that the thicknesses in which closure quadrants may occur are within the range of 15 to 36 nm. Thinner PTO tends to be fully strained without obvious domain structures, whereas thicker PTO tends to form alternating a/c domains (*21*) (figs. S13 to S16). In the present PTO/STO multilayer structures, each layer of PTO could be composed of such periodic closure quadrants. For example, in Fig. 4A, each of the two PTO layers is ~20 nm thick, and both layers contain the periodic closure quadrants. This indicates that, by repeatedly introducing STO layers, it is possible to fabricate extremely thick PTO/STO films that are composed of periodic disclination pairs in all PTO sublayers. Meanwhile, we find that the period of the closure-quadrant array w is strongly correlated with the PTO thickness d (Fig. 4C, following a linear relationship). In particular, for each PTO thickness, the ratio of period/thickness is ~1.45; i.e., $w \approx \sqrt{2}d$.

According to Kittel's law, stripe-domain widths are predominantly determined by the bulk domain energy E_d, the domain-wall energy E_w, and the film thickness d (*11*, *37*). This law was further extended for all ferroics, and a universal square root dependence $w \propto \sqrt{d}$ was deduced (*11*, *38*), where w is the domain period. However, the situation in the present study cannot be understood as simple 90°/180° stripe domains (*37*, *38*) because of the substantial nonuniform disclination strains that result from the configuration of the flux closures. In (*39*) it was theoretically demonstrated that, for films with a specific thickness range, the energy associated with disclination strains breaks the square root law, and a new linear law $w \propto \alpha + \beta d$ (where α and β are experiment-determined specific coefficients) is preferred. Our experimental results support the linear law with $\alpha = 0$ and $\beta = \sqrt{2}$.

Our results indicate that giant strain gradients can be preserved within a very thick PTO/STO film by simply increasing the PTO/STO period. This may provide opportunities for exploring various functionalities induced by strain gradients—such as the catalytic efficiency (*40*) of perovskite oxides—and other material properties that are tunable by elastic strains (*41*).

The results also extend the potential of employing epitaxial strain for modulating ferroelectric domain patterns. Designs based on controllable ferroelectric closure quadrants could be fabricated for investigating their dynamics and flexoelectric responses and, in turn, may assist future development of nanoscale ferroelectric devices such as high-density memories and high-performance energy-harvesting devices.

REFERENCES AND NOTES

1. J. F. Scott, Applications of modern ferroelectrics. *Science* **315**, 954–959 (2007). Medline doi:10.1126/science.1129564
2. I. I. Naumov, L. Bellaiche, H. Fu, Unusual phase transitions in ferroelectric nanodisks and nanorods. *Nature* **432**, 737–740 (2004). Medline doi:10.1038/nature03107
3. I. Kornev, H. Fu, L. Bellaiche, Ultrathin films of ferroelectric solid solutions under a residual depolarizing field. *Phys. Rev. Lett.* **93**, 196104 (2004). Medline doi:10.1103/PhysRevLett.93.196104
4. P. Aguado-Puente, J. Junquera, Ferromagneticlike closure domains in ferroelectric ultrathin films: First-principles simulations. *Phys. Rev. Lett.* **100**, 177601 (2008). Medline doi:10.1103/PhysRevLett.100.177601
5. B.-K. Lai, I. Ponomareva, I. I. Naumov, I. Kornev, H. Fu, L. Bellaiche, G. J. Salamo,

Electric-field-induced domain evolution in ferroelectric ultrathin films. *Phys. Rev. Lett.* **96**, 137602 (2006). Medline doi:10.1103/PhysRevLett.96.137602
6. I. Naumov, H. Fu, Vortex-to-polarization phase transformation path in ferroelectric $Pb(ZrTi)O_3$ nanoparticles. *Phys. Rev. Lett.* **98**, 077603 (2007). Medline doi:10.1103/PhysRevLett.98.077603
7. W. J. Chen, Y. Zheng, B. Wang, Vortex domain structure in ferroelectric nanoplatelets and control of its transformation by mechanical load. *Sci. Rep.* **2**, 00796 (2012). doi:10.1038/srep00796
8. T. Shinjo, T. Okuno, R. Hassdorf, K. Shigeto, T. Ono, Magnetic vortex core observation in circular dots of permalloy. *Science* **289**, 930–932 (2000). Medline doi:10.1126/science.289.5481.930
9. N. Romming, C. Hanneken, M. Menzel, J. E. Bickel, B. Wolter, K. von Bergmann, A. Kubetzka, R. Wiesendanger, Writing and deleting single magnetic skyrmions. *Science* **341**, 636–639 (2013). Medline doi:10.1126/science.1240573
10. N. Nagaosa, Y. Tokura, Topological properties and dynamics of magnetic skyrmions. *Nat. Nanotechnol.* **8**, 899–911 (2013). Medline doi:10.1038/nnano.2013.243
11. G. Catalan, J. Seidel, R. Ramesh, J. F. Scott, Domain wall nanoelectronics. *Rev. Mod. Phys.* **84**, 119–156 (2012). doi:10.1103/RevModPhys.84.119
12. C. Kittel, Physical theory of ferromagnetic domains. *Rev. Mod. Phys.* **21**, 541–583 (1949). doi:10.1103/RevModPhys.21.541
13. A. Schilling, D. Byrne, G. Catalan, K. G. Webber, Y. A. Genenko, G. S. Wu, J. F. Scott, J. M. Gregg, Domains in ferroelectric nanodots. *Nano Lett.* **9**, 3359–3364 (2009). Medline doi:10.1021/nl901661a
14. L. J. McGilly, A. Schilling, J. M. Gregg, Domain bundle boundaries in single crystal $BaTiO_3$ lamellae: Searching for naturally forming dipole flux-closure/quadrupole chains. *Nano Lett.* **10**, 4200–4205 (2010). Medline doi:10.1021/nl102566y
15. R. G. P. McQuaid, L. J. McGilly, P. Sharma, A. Gruverman, J. M. Gregg, Mesoscale flux-closure domain formation in single-crystal $BaTiO_3$. *Nat. Commun.* **2**, 404 (2011). doi:10.1038/ncomms1413
16. R. G. P. McQuaid, A. Gruverman, J. F. Scott, J. M. Gregg, Exploring vertex interactions in ferroelectric flux-closure domains. *Nano Lett.* **14**, 4230–4237 (2014). Medline doi:10.1021/nl5006788
17. L. J. McGilly, J. M. Gregg, Polarization closure in $PbZr_{(0.42)}Ti_{(0.58)}O_3$ nanodots. *Nano Lett.* **11**, 4490–4495 (2011). Medline doi:10.1021/nl2031103
18. L.-W. Chang, V. Nagarajan, J. F. Scott, J. M. Gregg, Self-similar nested flux closure structures in a tetragonal ferroelectric. *Nano Lett.* **13**, 2553–2557 (2013). Medline doi:10.1021/nl400629m
19. C.-L. Jia, K. W. Urban, M. Alexe, D. Hesse, I. Vrejoiu, Direct observation of continuous electric dipole rotation in flux-closure domains in ferroelectric $Pb(Zr,Ti)O_3$. *Science* **331**, 1420–1423 (2011). Medline doi:10.1126/science.1200605
20. C. T. Nelson, B. Winchester, Y. Zhang, S. J. Kim, A. Melville, C. Adamo, C. M. Folkman, S. H. Baek, C. B. Eom, D. G. Schlom, L. Q. Chen, X. Pan, Spontaneous vortex nanodomain arrays at ferroelectric heterointerfaces. *Nano Lett.* **11**, 828–834 (2011). Medline doi:10.1021/nl1041808
21. G. Catalan, A. Lubk, A. H. Vlooswijk, E. Snoeck, C. Magen, A. Janssens, G. Rispens, G. Rijnders, D. H. Blank, B. Noheda, Flexoelectric rotation of polarization in ferroelectric thin films. *Nat. Mater.* **10**, 963–967 (2011). Medline doi:10.1038/nmat3141
22. C. L. Jia, S. B. Mi, K. Urban, I. Vrejoiu, M. Alexe, D. Hesse, Atomic-scale study of electric dipoles near charged and uncharged domain walls in ferroelectric films. *Nat. Mater.* **7**, 57–61 (2008). Medline doi:10.1038/nmat2080
23. Y. L. Tang, Y. L. Zhu, Y. J. Wang, W. Y. Wang, Y. B. Xu, W. J. Ren, Z. D. Zhang, X. L. Ma, Atomic-scale mapping of dipole frustration at 90° charged domain walls in ferroelectric $PbTiO_3$ films. *Sci. Rep.* **4**, 04115 (2014). doi:10.1038/srep04115
24. P. Gao, J. Britson, J. R. Jokisaari, C. T. Nelson, S.-H. Baek, Y. Wang, C.-B. Eom, L.-Q. Chen, X. Pan, Atomic-scale mechanisms of ferroelastic domain-wall-mediated ferroelectric switching. *Nat. Commun.* **4**, 3791 (2013). doi:10.1038/ncomms3791
25. N. Balke, S. Choudhury, S. Jesse, M. Huijben, Y. H. Chu, A. P. Baddorf, L. Q. Chen, R. Ramesh, S. V. Kalinin, Deterministic control of ferroelastic switching in multiferroic materials. *Nat. Nanotechnol.* **4**, 868–875 (2009). Medline doi:10.1038/nnano.2009.293
26. N. Balke, B. Winchester, W. Ren, Y. H. Chu, A. N. Morozovska, E. A. Eliseev, M. Huijben, R. K. Vasudevan, P. Maksymovych, J. Britson, S. Jesse, I. Kornev, R. Ramesh, L. Bellaiche, L. Q. Chen, S. V. Kalinin, Enhanced electric conductivity at ferroelectric vortex cores in $BiFeO_3$. *Nat. Phys.* **8**, 81–88 (2012). doi:10.1038/nphys2132
27. Materials and methods are available as supplementary materials on *Science* Online.
28. S. M. Anthony, S. Granick, Image analysis with rapid and accurate two-dimensional Gaussian fitting. *Langmuir* **25**, 8152–8160 (2009). Medline doi:10.1021/la900393v
29. M. J. Hÿtch, E. Snoeck, R. Kilaas, Quantitative measurement of displacement and strain fields from HREM micrographs. *Ultramicroscopy* **74**, 131–146 (1998). doi:10.1016/S0304-3991(98)00035-7
30. D. J. Srolovitz, J. F. Scott, Clock-model description of incommensurate ferroelectric films and of nematic-liquid-crystal films. *Phys. Rev. B* **34**, 1815–1819 (1986). doi:10.1103/PhysRevB.34.1815
31. A. K. Tagantsev, L. E. Cross, J. Fousek, in *Domains in Ferroic Crystals and Thin Films* (Springer, New York, 2010), chap. 6, pp. 300–304.
32. A. K. Tagantsev, Electric polarization in crystals and its response to thermal and elastic perturbations. *Phase Transit.* **35**, 119–203 (1991). doi:10.1080/01411599108213201
33. Y. Liu, G. Xu, C. Song, Z. Ren, G. Han, Y. Zheng, First-principles study of elastic properties in perovskite $PbTiO_3$. *Mater. Sci. Eng. A* **472**, 269–272 (2008). doi:10.1016/j.msea.2007.03.028
34. A. G. Kalinichev, J. D. Bass, B. N. Sun, D. A. Payne, Elastic properties of tetragonal $PbTiO_3$ single crystals by Brillouin scattering. *J. Mater. Res.* **12**, 2623–2627 (1997). doi:10.1557/JMR.1997.0349
35. G. C. C. Costa, P. Saradhi Maram, A. Navrotsky, Thermodynamics of nanoscale lead titanate and barium titanate perovskites. *J. Am. Ceram. Soc.* **95**, 3254–3262 (2012). doi:10.1111/j.1551-2916.2012.05373.x
36. N. D. Mermin, The topological theory of defects in ordered media. *Rev. Mod. Phys.* **51**, 591–648 (1979). doi:10.1103/RevModPhys.51.591
37. C. Kittel, Theory of the structure of ferromagnetic domains in films and small particles. *Phys. Rev.* **70**, 965–971 (1946). doi:10.1103/PhysRev.70.965
38. A. L. Roitburd, Equilibrium structure of epitaxial layers. *Phys. Status Solidi A* **37**, 329–339 (1976). doi:10.1002/pssa.2210370141
39. N. A. Pertsev, A. G. Zembilgotov, Energetics and geometry of 90° domain structures in epitaxial ferroelectric and ferroelastic films. *J. Appl. Phys.* **78**, 6170–6180 (1995). doi:10.1063/1.360561
40. J. Suntivich, K. J. May, H. A. Gasteiger, J. B. Goodenough, Y. Shao-Horn, A perovskite oxide optimized for oxygen evolution catalysis from molecular orbital principles. *Science* **334**, 1383–1385 (2011). Medline doi:10.1126/science.1212858
41. D. Yu, J. Feng, J. Hone, Elastically strained nanowires and atomic sheets. *MRS Bull.* **39**, 157–162 (2014). doi:10.1557/mrs.2014.6
42. K. J. Choi, M. Biegalski, Y. L. Li, A. Sharan, J. Schubert, R. Uecker, P. Reiche, Y. B. Chen, X. Q. Pan, V. Gopalan, L. Q. Chen, D. G. Schlom, C. B. Eom, Enhancement of ferroelectricity in strained $BaTiO_3$ thin films. *Science* **306**, 1005–1009 (2004). Medline doi:10.1126/science.1103218
43. J. H. Lee, L. Fang, E. Vlahos, X. Ke, Y. W. Jung, L. F. Kourkoutis, J. W. Kim, P. J. Ryan, T. Heeg, M. Roeckerath, V. Goian, M. Bernhagen, R. Uecker, P. C. Hammel, K. M. Rabe, S. Kamba, J. Schubert, J. W. Freeland, D. A. Muller, C. J. Fennie, P. Schiffer, V. Gopalan, E. Johnston-Halperin, D. G. Schlom, A strong ferroelectric ferromagnet created by means of spin-lattice coupling. *Nature* **466**, 954–958 (2010). Medline doi:10.1038/nature09331
44. M. D. Biegalski, J. H. Haeni, S. Trolier-McKinstry, D. G. Schlom, C. D. Brandle, A. J. V. Graitis, Thermal expansion of the new perovskite substrates $DyScO_3$ and $GdScO_3$. *J. Mater. Res.* **20**, 952–958 (2005). doi:10.1557/JMR.2005.0126
45. O. Chaix-Pluchery, D. Sauer, J. Kreisel, Temperature-dependent Raman scattering of $DyScO_3$ and $GdScO_3$ single crystals. *J. Phys. Condens. Matter* **22**, 165901 (2010). Medline doi:10.1088/0953-8984/22/16/165901
46. C. L. Jia, V. Nagarajan, J. Q. He, L. Houben, T. Zhao, R. Ramesh, K. Urban, R. Waser, Unit-cell scale mapping of ferroelectricity and tetragonality in epitaxial ultrathin ferroelectric films. *Nat. Mater.* **6**, 64–69 (2007). Medline doi:10.1038/nmat1808
47. S. Bals, S. Van Aert, G. Van Tendeloo, D. Ávila-Brande, Statistical estimation of atomic positions from exit wave reconstruction with a precision in the picometer range. *Phys. Rev. Lett.* **96**, 096106 (2006). Medline doi:10.1103/PhysRevLett.96.096106
48. S. Van Aert, S. Turner, R. Delville, D. Schryvers, G. Van Tendeloo, E. K. Salje, Direct observation of ferrielectricity at ferroelastic domain boundaries in $CaTiO_3$ by electron microscopy. *Adv. Mater.* **24**, 523–527 (2012). Medline doi:10.1002/adma.201103717

49. A. K. Tagantsev, G. Gerra, N. Setter, Short-range and long-range contributions to the size effect in metal-ferroelectric-metal heterostructures. *Phys. Rev. B* **77**, 174111 (2008). doi:10.1103/PhysRevB.77.174111
50. M. J. Hÿtch, J.-L. Putaux, J.-M. Pénisson, Measurement of the displacement field of dislocations to 0.03 Å by electron microscopy. *Nature* **423**, 270–273 (2003). Medline doi:10.1038/nature01638
51. J. Slutsker, A. Artemev, A. Roytburd, Phase-field modeling of domain structure of confined nanoferroelectrics. *Phys. Rev. Lett.* **100**, 087602 (2008). Medline doi:10.1103/PhysRevLett.100.087602
52. A. J. Bell, Phenomenologically derived electric field-temperature phase diagrams and piezoelectric coefficients for single crystal barium titanate under fields along different axes. *J. Appl. Phys.* **89**, 3907 (2001). doi:10.1063/1.1352682
53. J. Hlinka, P. Márton, Phenomenological model of a 90° domain wall in $BaTiO_3$-type ferroelectrics. *Phys. Rev. B* **74**, 104104 (2006). doi:10.1103/PhysRevB.74.104104
54. P. Marton, I. Rychetsky, J. Hlinka, Domain walls of ferroelectric $BaTiO_3$ within the Ginzburg-Landau-Devonshire phenomenological model. *Phys. Rev. B* **81**, 144125 (2010). doi:10.1103/PhysRevB.81.144125
55. W. Ma, L. E. Cross, Flexoelectricity of barium titanate. *Appl. Phys. Lett.* **88**, 232902 (2006). doi:10.1063/1.2211309
56. I. Ponomareva, A. K. Tagantsev, L. Bellaiche, Finite-temperature flexoelectricity in ferroelectric thin films from first principles. *Phys. Rev. B* **85**, 104101 (2012). doi:10.1103/PhysRevB.85.104101

ACKNOWLEDGMENTS

This work is supported by the National Natural Science Foundation of China (grants 51231007 and 51171190) and the National Basic Research Program of China (grants 2014CB921002 and 2009CB623705). A.N.M. and E.A.E. acknowledge financial support from the National Academy of Science of the Ukraine; A.Y.B. and S.J.P. thank the U.S. Department of Energy, Office of Basic Energy Sciences, Materials Sciences and Engineering Division for financial support. The authors at SYNL are grateful to B. Wu and L. X. Yang of this laboratory for their technical support on the Titan platform of the aberration-corrected scanning transmission electron microscope. Author contributions: Y.L.Z. and X.L.M. conceived the project of interfacial characterization in oxides by using aberration-corrected STEM; Y.L.T. performed the thin-film growth and TEM observations; W.Y.W. provided some of the TEM images used in the supplementary materials; Y.J.W. carried out digital analysis of the STEM data; Y.B.X. and Z.D.Z. contributed to the thin-film growth; A.N.M. and E.A.E. participated in the ferroelectric theoretical analysis based on the LGD framework; and A.Y.B. and S.J.P. contributed to STEM-HAADF imaging data analysis, particularly to the calculation of the strain-gradient components near the vertex core. All authors participated in discussion and interpretation of the data. Correspondence and requests for materials should be addressed to X.L.M.

SUPPLEMENTARY MATERIALS

www.sciencemag.org/cgi/content/full/science.1259869/DC1
Materials and Methods
Supplementary Text
Figs. S1 to S16
Table S1
References (*42*–*56*)

11 August 2014; accepted 24 March 2015
Published online 16 April 2015
10.1126/science.1259869

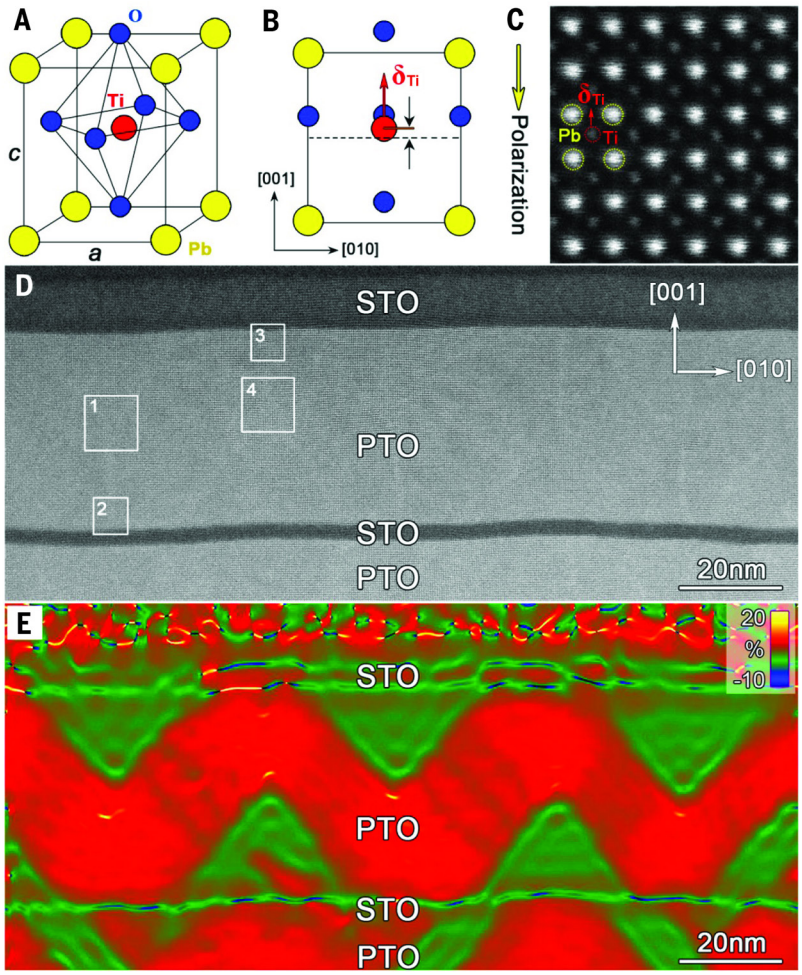

Fig. 1. Long-range periodic disclination pairs in a ferroelectric $PbTiO_3$ layer. (**A**) Schematic perspective view of the unit cell of $PbTiO_3$ (yellow, Pb; red, Ti; blue, O). (**B**) Projection of the unit cell along the [100] direction. (**C**) HAADF-STEM image of the $PbTiO_3$ crystal along [100]. (**D**) Low-magnification high-resolution HAADF-STEM image showing the upper $PbTiO_3$ layer in a $SrTiO_3$(10 nm)/$PbTiO_3$(36 nm)/$SrTiO_3$(3 nm)/$PbTiO_3$(28 nm)/$GdScO_3$ multilayer. Boxes labeled with numbers 1 to 4 denote typical areas. (**E**) GPA analysis of the STEM data reveals the out-of-plane strain ε_{yy}. The *c* domains are associated with an abrupt elongation of the out-of-plane lattice parameter (red areas) and exhibit a sinusoidal array. The domains (in green), with triangular head-to-head configurations having a smaller ε_{yy}, are *a* domains.

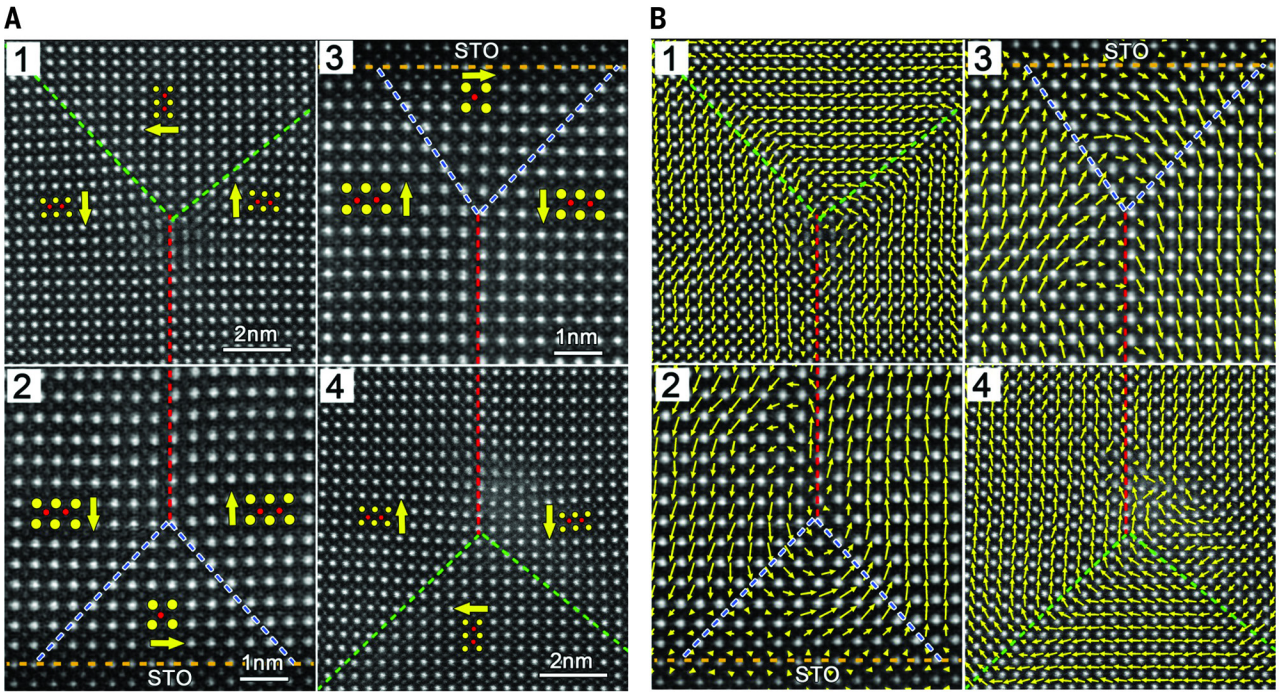

Fig. 2. Superposition of HAADF-STEM images and Ti^{4+} displacement vector maps showing the closure quadrants. (**A**) Atomically resolved HAADF-STEM images corresponding to the areas labeled as 1, 2, 3, and 4 in Fig. 1D. The red and yellow circles denote the positions of Ti^{4+} and Pb^{2+} columns, respectively. Arrows denote reversed Ti^{4+} displacement directions. (**B**) Superposition of reversed δ_{Ti} vectors with experimental images. The δ_{Ti} vectors corresponding to PTO unit cells are shown as yellow arrows superimposed on the atomic image of Fig. 2A. The green and blue dashed lines indicate the 90° domain walls in areas 1 and 4, as well as 2 and 3, respectively. The red dashed lines indicate the 180° domain walls.

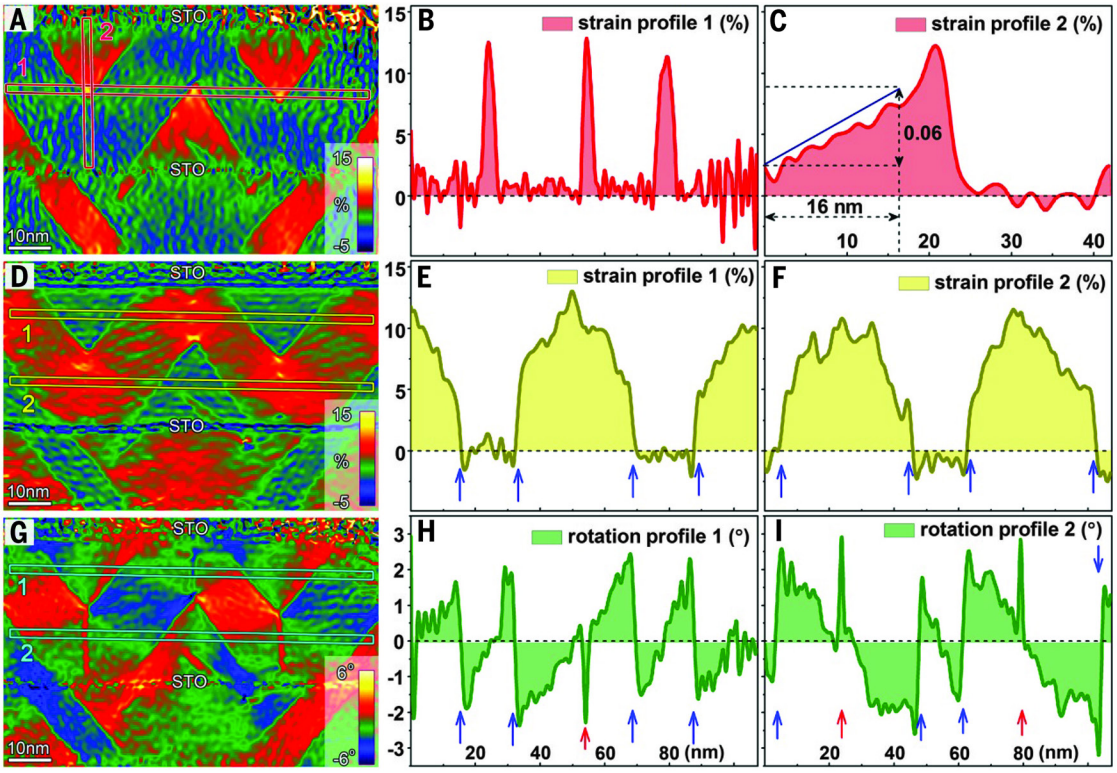

Fig. 3. Strain mappings of the periodic disclination pairs. (**A** to **C**) In-plane strain (ε_{xx}) maps and corresponding line profiles of areas 1 and 2 [labeled in (A)]. (**D** to **F**) Out-of-plane strain (ε_{yy}) maps and corresponding line profiles of areas 1 and 2 [labeled in (D)]. (**G** to **I**) Lattice rotation maps and corresponding line profiles of areas 1 and 2 [labeled in (G)]. Note the very inhomogeneous distribution of the strains and lattice rotations. The continuous, giant *c* lattice strain gradient estimated in the triangle domain in (C) is ~4 × 10^6 m^{-1}. Blue arrows in (E), (F), (H), and (I) denote the strain-rotation abrupt change points indicating the 90° domain walls. Red arrows in (H) and (I) denote the rotation maximal points indicating the 180° domain walls.

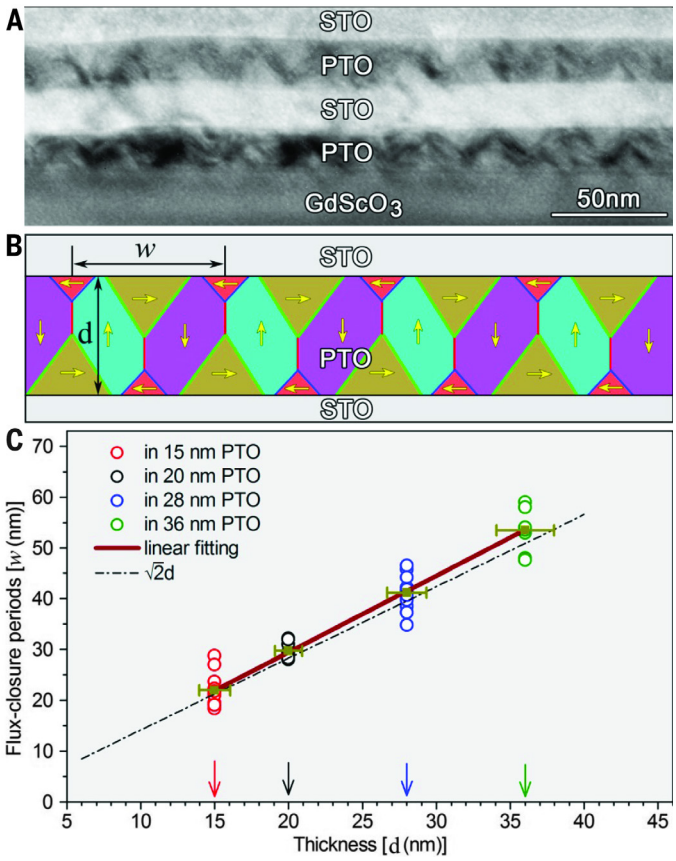

Fig. 4. Variation of flux-closure period with $PbTiO_3$ thicknesses. (**A**) Cross-sectional TEM image showing an overview of a $SrTiO_3$(10 nm)/$PbTiO_3$(20 nm)/$SrTiO_3$(20 nm)/$PbTiO_3$(20 nm)/$GdScO_3$ multilayer. Two flux-closure arrays align periodically in both $PbTiO_3$ layers. (**B**) Schematic showing the flux-closure domain configuration based on the experimental data in Figs. 1 to 3. Because not all of the 90° domain walls in Fig. 2A are visible in the strain maps, the 90° domain walls were denoted by green (visible) and blue (invisible) dashed lines, respectively. (**C**) Linear relationship between the thicknesses (*d*) and the periods (*w*) of closure-quadrant arrays in $PbTiO_3$ layers on $GdScO_3$. The linear fit is close to $\sqrt{2}d$.